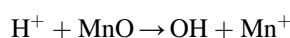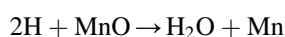# Manganese Production with Hydrogen Plasma

Trygve Storm Aarnæs, Roar Jensen, Sverre Gullikstad Johnsen, and Halvor Dalaker

Abstract

Hydrogen (H_2) gas has been proposed as an attractive candidate to replace carbon in metal production. Oxide reduction with H_2 releases water (H_2O) as the off-gas rather than carbon dioxide (CO_2). This has been shown to be feasible, for e.g., iron oxides and some manganese oxides. However, common, more stable oxides, such as manganese monoxide (MnO), are subject to thermodynamic limitations, which prohibit reduction with H_2. Utilizing monoatomic or ionized hydrogen (H or H^+), abundant in hydrogen plasma, makes the hydrogen-oxide reactions more favorable and allows reactions such as:

$$2H + MnO \rightarrow H_2O + Mn$$

$$H^+ + MnO \rightarrow OH + Mn^+$$

The current work demonstrates experimentally the production of metallic manganese by exposing sintered MnO to hydrogen plasma. The hydrogen plasma was generated by passing H_2 through a plasma torch. This paper will present the experimental setup and method, as well as characterization of the reaction products. Hypotheses for the reaction paths are presented and discussed in the context of thermodynamics and solidification theory. Furthermore, computational fluid dynamics is used to support the discussions via mathematical modeling of temperature- and flow fields.

Although substantial research is still needed, the presented results demonstrate that hydrogen plasma allows for reduction of more stable oxides than is possible with H_2, and that hydrogen plasma-based technologies can be used for manganese production.
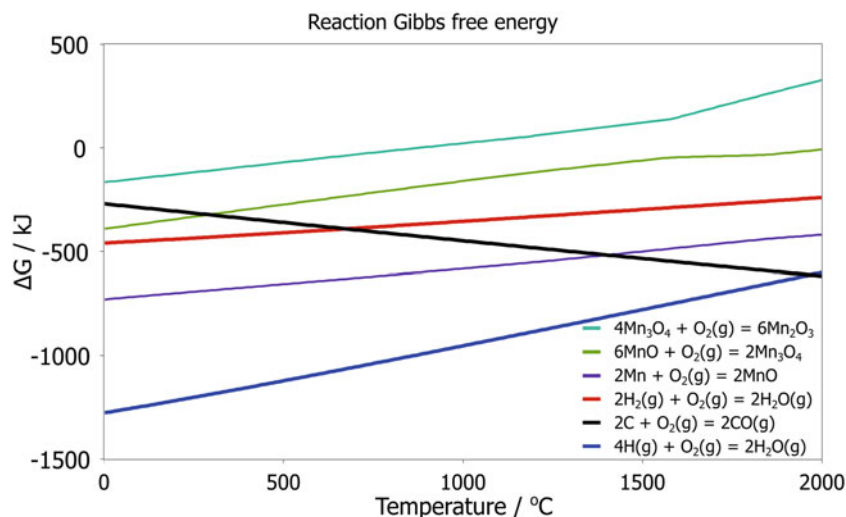
1   Introduction

The production of metals from oxide raw materials is a major source of CO_2 emissions, largely due to the reduction reaction between the metal oxides and carbon. This process is illustrated by Eq. (1).

$$2MeO + C = Me + CO_2 \tag{1}$$

T. S. Aarnæs (✉) · R. Jensen · S. G. Johnsen · H. Dalaker
SINTEF Industry, Trondheim, Norway
e-mail: trygve.aarnaes@sintef.no

Fig. 1 Change in Gibbs free energy for the reduction of manganese oxides, along with H_2O and CO. Because the reduction of MnO has a higher change in Gibbs energy than H_2, it cannot be reduced by H_2. Calculated in HSC 9

Due to these process-related emissions, decarbonizing the electricity grid will not be sufficient to fully decarbonize metal production. The process-related emissions must also be addressed. An often discussed option is replacing carbon in Eq. (1) with hydrogen. The resulting reaction is shown below in Eq. (2):

$$2MeO + H_2 = Me + H_2O \tag{2}$$

Replacing carbon with hydrogen as the reductant has the potential to significantly reduce CO_2 emissions, since the by-product of the reaction is harmless water vapor. While hydrogen-based processes have been successfully developed for certain metals (e.g., iron), they remain a challenge for others, including manganese [1, 2]. This is due to hydrogen's lower potency as a reductant compared to carbon at high temperatures, as shown in Fig. 1. While hydrogen can reduce manganese oxides to MnO, it lacks the potency to produce metallic manganese, highlighting the need for innovative approaches for hydrogen utilization in manganese production.

Exciting H_2 to the plasma state generates a number of new species such as monoatomic hydrogen (H), rotationally/vibrationally excited hydrogen (H_2^*), and ionic hydrogen (H_2^+ and H^+). These species are known to be highly reactive [3, 4]. In the case of manganese production, converting H_2 into hydrogen plasma prior to using it as a reductant, corresponds to shifting the line for H_2 in Fig. 1 toward the line of monoatomic hydrogen, which could result in the reduction of MnO to metallic manganese becoming feasible.

Industrial manganese production currently relies on carbon-based processes which contribute to greenhouse gas emissions. However, a hydrogen plasma-based process would make it possible to replace carbon with electricity and hydrogen. If successfully developed, this technology has the potential to enable completely CO_2-free manganese production, as long as the required electricity and hydrogen come from carbon-neutral sources.

Natural gas reforming is currently the dominating production method for hydrogen. This process results in what is known as "gray" hydrogen and is associated with substantial CO_2 emissions. Hydrogen produced in alternative, CO_2-free processes include, e.g., "blue" and "turquoise" variants, produced from natural gas with carbon capture and through thermal cracking, respectively. "Green" hydrogen can be produced via electrolysis of water, but is much more costly, in terms of electrical energy input, compared with the "blue" and "turquoise" alternatives [5]. Hydrogen is one possible solution for decarbonizing several industrial processes, since it has the potential to replace carbon both as fuel/heating source and as a reducing agent. There are concerns, however, that the increasing interest in hydrogen-based processes will result in hydrogen shortage [6]. Although, the hydrogen supply may be insufficient to realize the full decarbonization potential across all industries, it is important that policy makers stimulate R&D activities to explore all possible routes toward carbon neutrality.

Building upon our team's previous work on a technoeconomic prefeasibility study of a hydrogen plasma-based ferromanganese plant [7], and success in generating small amounts of manganese with hydrogen plasma using an arc melter [8], the present work aims to upscale the process into the hundreds of grams range by utilizing a specially designed plasma reactor. In the following sections, we describe the development of this custom-built reactor, including expected temperature and flow profiles, followed by a detailed investigation of the plasma-based production of manganese.

Fig. 2 Crucibles loaded with MnO raw material for each of the experiments. Experiments 1 and 2 used pure MnO, while experiment 3 used 15 wt.% iron and 85 wt.% MnO

2 Experimental Details

The experimental work described in this paper covers three experiments where MnO reduction with hydrogen plasma was attempted. The first experiment used disks (Ø = 27 mm) of pure MnO stacked on top of each other resembling a tower. The results from this experiment have been accepted for publication at a different conference [9]. In the second experiment, larger pieces of pure MnO were used, and the crucible was fully charged. The third experiment used a mixture of 15 wt.% metallic iron and 85 wt.% MnO. Figure 2 shows the loaded crucible for each experiment.

2.1 Materials

The raw materials used in this experimental work was 99% pure MnO and 99% pure iron powder supplied by Thermo Fischer Scientific.

The powders could not be used directly in the reactor because the high velocity of the plasma jet fluidizes and ejects the powdery materials from the crucible. Spark Plasma Sintering (SPS) was used to agglomerate the powders into larger pieces that could be used in the reactor. SPS uses a graphite pressing tool lined with graphite paper to compress the powders while an electrical current goes through the pressing tool to generate heat.

SPS was done in a vacuum, which made it possible to detect if the graphite tool reduced MnO, since the CO released from this reaction will cause a pressure increase. This was not seen. The position of the press indicates when sintering is finished because MnO undergoes a volume reduction during sintering. The MnO powders were sintered at 250 MPa pressure and 900 °C for approximately 30 minutes. After sintering, the graphite paper was removed by sandblasting.

2.2 Plasma Equipment

A custom-built reactor was used to carry out the current experimental work. The main parts of the reactor are a cylindrical vessel, a plasma torch mounted on the reactor lid, and a copper crucible mounted directly below the plasma torch (see Fig. 3a). All reactor surfaces were water-cooled. The temperature and flow-rates were monitored for each cooling water circuit, separately. These were used to calculate the individual coolant circuits' heat uptake, e.g., in the crucible and the plasma torch. In addition, the reactor is equipped with a camera aimed at the crucible, which provides a video feed of the sample throughout each experiment.

The plasma torch, equipped with a tungsten cathode and a copper nozzle/anode, was operated in nontransferred arc mode. The electric arc burns between the cathode and the nozzle/anode and heats gas, which is flowing in the annulus between the cathode and anode, transforming it into a plasma jet. The hot plasma gas flows over the sample charged in the crucible, melting it, and reacting with it.

Fig. 3 (**a**) Schematic drawing of the custom-built plasma reactor used in the current experiments, and (**b**) axisymmetric representation used in numerical simulations
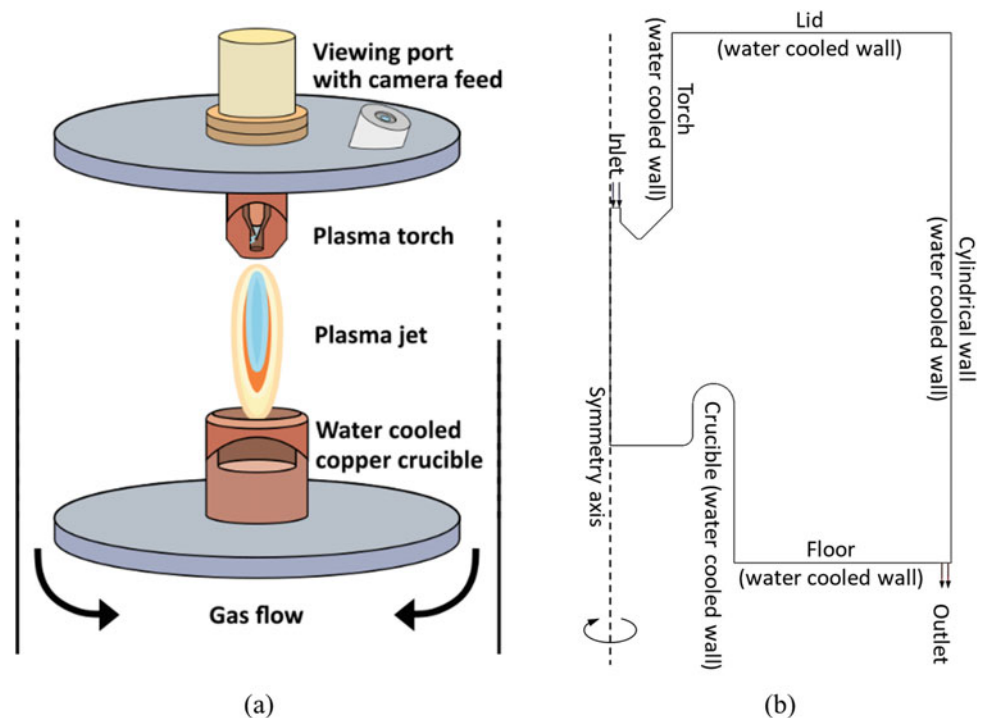
2.3   Experimental Procedure

After charging the crucible, the reactor chamber was evacuated and purged with argon (Ar), prior to plasma torch ignition. During start-up, Ar was used as the plasma gas due to its high electrical conductivity, which makes ignition easier. The H_2 content was gradually increased. The plasma torch was run with 300 A electric current, and the power output is dependent on the plasma gas composition due to the various gasses' different electric conductivities. E.g., by increasing the H_2 content of the plasma gas, the power output increased. To avoid overheating the sample, it was monitored through the camera feed.

2.4   Analysis

Samples from the crucible were taken after each experiment and were cast in epoxy and polished in preparation for analysis in SEM. The chemical composition of the different phases was determined using EDS (electron dispersive x-ray spectroscopy) and EPMA (electron probe microanalysis).

3   Numerical Modeling

Numerical simulations (Computational Fluid Dynamics, CFD) were employed to shed light on the nature of flow- and temperature fields inside the reactor chamber. Using default settings, laminar,[1] steady-state simulations with the DO radiation model activated, were performed in ANSYS Fluent 2022R1 [10]. The simulated geometry was based on a simplified, axisymmetric 2D representation of the reactor chamber and an empty crucible (see Fig. 3b). The computational mesh consisted of 36 thousand 1 mm-sized quadrilateral cells. Refining the mesh resulted in minor quantitative changes in the flow- and temperature fields, only. Walls were modeled as no-slip, constant temperature boundaries with emissivity of 1. Their individual temperatures were estimated based on the monitored coolant temperatures and total heat loss and were in the range of 280–285 K. The outlet was modeled by a prescribed pressure of 0 Pa(g). The plasma gas inlet was modeled by constant velocity and temperature. The inlet temperature (6100 K) was set so that the combined enthalpy flow and radiation from the

---

[1] Simulation with the kω SST turbulence model revealed that turbulence effects were mostly negligible (turbulent visosity ratio < 1 everywhere).

Fig. 4 Results from simulations: (**a**) Velocity contours and vectors; (**b**) temperature contours. The black and red curves represent isotherms for the melting (outer) and boiling (inner) points of Mn (1519 K and 2334 K) and MnO (2218 K and 3400 K), respectively
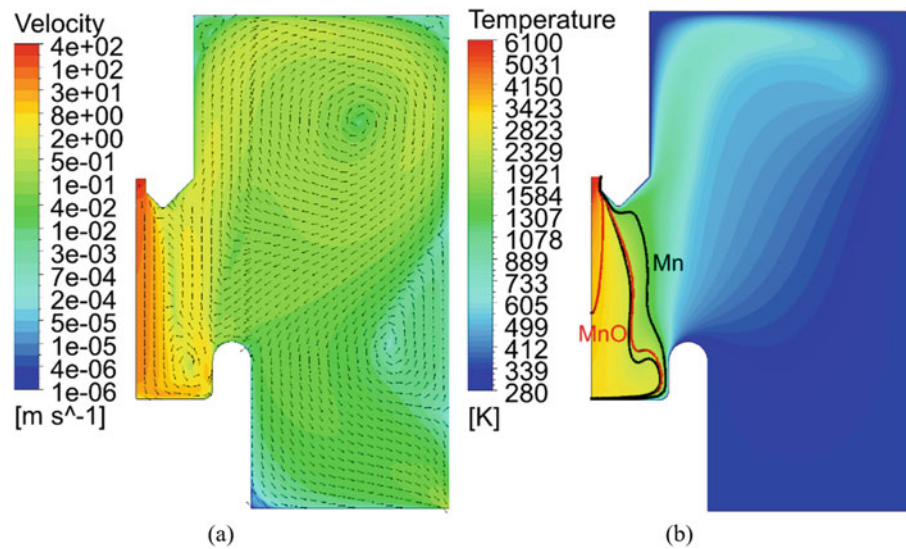
inlet approximated an electric arc power of 24 kW. The inlet velocity (334 m/s) corresponded to the total flow-rate of 40 standard liters per minute.[2] For simplicity, it was assumed that the plasma gas was pure hydrogen, and its temperature-dependent gas material properties were obtained from Boulos and Pfender [11] under the assumption of local thermodynamic equilibrium everywhere. The net absorption coefficient was obtained from Liani et al. [12].

4   Results and Discussion

4.1   Numerical Simulations

Sample simulation results are provided in Fig. 4, where velocity contours and vectors and temperature contours are shown. Due to limited information about local cooling rates along the reactor wall boundaries, the simulations can only be expected to give a coarse impression of flow- and temperature conditions inside the reactor. E.g., it is expected that the inlet temperature is exaggerated since no cooling inside the torch was considered, and because average wall temperatures were used, simulated local cooling rates are inaccurate.

The simulation suggests that a high-temperature region ($T > 1500$ K) only exists in the region between the torch and the crucible. Large recirculation zones form inside the reactor chamber, which contribute to efficient cooling of the high-temperature zone and cause the gas to meander toward the outlet. At the outlet, the gas has the same temperature as the coolant, which corresponds well with the observed temperatures in the downstream gas cooling system.

To assess the effect of mixing hydrogen gas with argon, the simulation was repeated with pure argon, maintaining the volumetric flow-rate of 40 slm and electric arc power of 24 kW. Argon material properties were obtained from Boulos and Pfender [11] and the net absorption coefficient was derived from Aubrecht et al. [13] as outlined by Johnsen and Simonsen [14]. The inlet velocity and temperature were set to 227 m/s and 8100 K, respectively. Whereas the inlet energy flux was dominated by convected enthalpy (~75%) for pure hydrogen, it was dominated by radiation (~80%) for pure argon. The main differences observed in the simulation results were the level of turbulence,[3] a more complex flow field, with additional recirculation zones, and a high-temperature plume that dominated the upper half of the reactor chamber. It should be kept in mind that for pure argon, the mass flow was almost 20 times higher than for pure hydrogen, at identical standard condition volume-flow.

---

[2]Torch operation parameters (e.g., flow-rate and power output) were selected to match "typical" operation parameter values from the experimental campaign.

[3]Using the kω SST turbulence model with pure argon, the turbulent viscosity ratio was above 10 in large parts of the reactor volume.

In the case that the crucible is not empty, but filled with raw material (see Fig. 2), the flow pattern may be affected considerably, and the extremely thin thermal boundary layer where the plasma jet hits the crucible floor directly, in the current simulations, will be dramatically affected. This will result in significantly reduced heat transfer through the crucible floor, depending on the effective thermal conductivity and thickness of the charge. It may thus be expected that the high-temperature zone will extend into the reactor chamber and more heat will be absorbed through the reactor lid and cylindrical side walls. Moreover, it can be seen that for the empty crucible, the plasma jet is forced upwards toward the top of the reactor, by the inner side walls of the crucible. The gas is cooled significantly due to heat loss through the crucible and outer torch walls. If the crucible is full, however, the jet will be deflected sideways instead of upwards, and the gas might take a more direct route toward the outlet. In this case, the cooling by the crucible and reactor walls will be less efficient, and higher temperatures can be expected at the gas outlet.

4.2   Operation of the Plasma Reactor

During the experiments, the flow of H_2 through the plasma torch and electric power was varied in order to achieve the desired amount of melt, and sometimes to remove condensate that was obstructing the view of the camera. The left column in Fig. 5 shows the flow of Ar and H_2 to the plasma torch and the electrical power as functions of time. The right column in Fig. 5 shows the heat uptake in the plasma torch and crucible cooling circuits along with the electrical power. Unsurprisingly, the heat uptake in the plasma torch follows the electrical power closely. However, for experiments 2 and 3, the heat uptake in the crucible is gradually increasing, even when the power is fixed, due to the slow removal of raw material.

Experiment 1   In this experiment, 140 g of raw material was used. The goal was to slowly liquefy the stack of MnO discs (see Fig. 2), and let the melt run down the sides and solidify. Due to the quite small amount of MnO used in this experiment, the heat transfer to the crucible corresponded closely with the electrical power. The H_2 fraction was slowly increased during the experiment to slowly melt through the MnO stack. The experiment was finished when the stack was melted approximately halfway through. The residual raw material can be seen in Fig. 6.

Experiment 2   By fully loading the crucible with 658 g of raw material, the goal was to maintain a melt of MnO. Due to experience from earlier experiments, there were concerns that too high power would result in evaporation and subsequent back-reaction of produced Mn, so the power was maintained at roughly 20 kW. The heat transfer to the crucible increased gradually over the course of the experiment, which shows that the plasma gas was pushing through the raw material. However, this rate was rather slow and left a considerable amount of remaining, unmelted raw material after the experiment, as can be seen in Fig. 6.

Experiment 3   This experiment utilized a raw material composed of 15 wt.% Fe and 85 wt.% MnO. The crucible was fully loaded with 659 g of raw material. The role of the iron was to lower the vapor pressure of manganese vapor and thus reduce evaporation losses. Additionally, it lowers the activity of manganese by producing a FeMn alloy. Increased electrical power was used during this experiment in an attempt to liquefy more of the raw material. This led to the plasma jet almost digging through the center of the raw material, which can also be seen by the comparatively rapid increase in heat uptake. Figure 6 shows the crucible and raw material after the experiment, much of the iron has coalesced into a large central drop, and there are smaller drops of iron surrounding it.

4.3   Reaction Products

Manganese Formation   Examinations with EPMA detected manganese formation. It was mainly found within the MnO that had been melted and then solidified. The manganese formation in Experiment 1 is already described elsewhere [9]. Figure 7a shows metallic manganese found within the molten MnO from Experiment 2. The amount of manganese formed in Experiment 2 appears greater than in Experiment 1, which can indicate that having large enough sample to sustain a melt is beneficial for the reduction. The observed formation of manganese is highly promising, as this shows that plasma can be used to increase the reducing power of H_2.
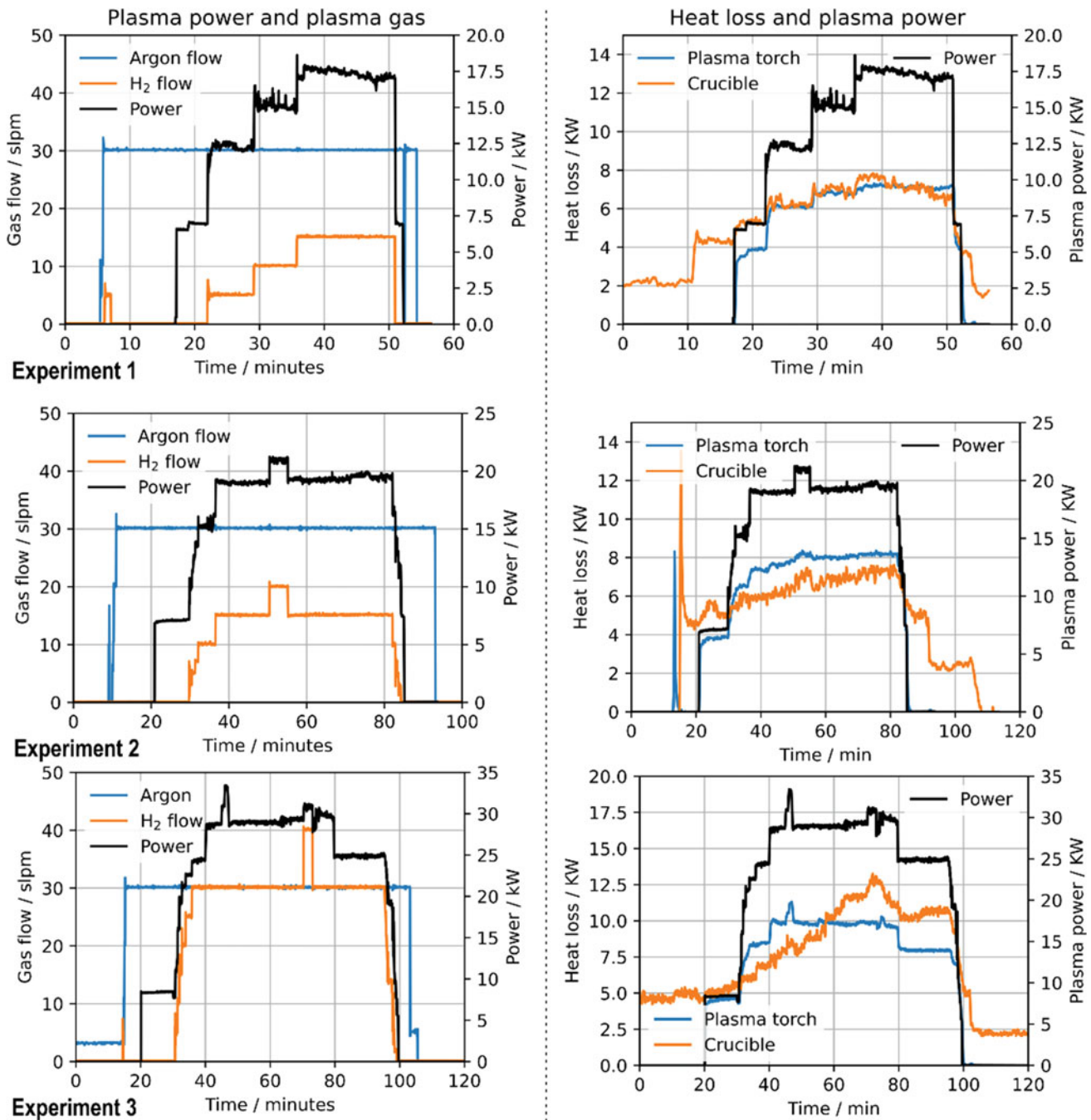
Fig. 5 The charts in the left column show the flow of H_2 and Ar gas through the plasma torch, and the electric power input for each of the experiments, and the charts in the right column show the heat uptake in the crucible and the plasma torch along with the electric power

The back-reaction of manganese is written in Eq. (3). This was a major concern, since the back-reaction is thermodynamically favored at all temperatures. The fact that manganese was mostly found within a matrix of MnO strengthens this concern, since it implies that most manganese on the surface of the MnO was oxidized by water.

$$Mn + H_2O = MnO + H_2 \tag{3}$$
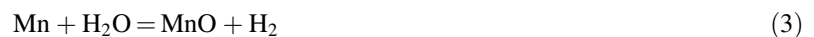
Manganese was also found within MnO particles that were scattered throughout the reactor. These particles were comprised of three parts: A hollow core, a layer of MnO with manganese along the MnO grain boundaries, and a surface layer that only contained MnO. Figure 6b shows an example of this type of particle. These particles must have either formed as manganese that back-reacted to MnO through a topochemical reaction mechanism, or they formed as MnO particles that were partially converted into metallic manganese.

In Experiment 3, a large part of the produced manganese was found in a FeMn alloy particle. Figure 7c shows BSE images of the metal particle. It was analyzed with EPMA and found to have a manganese content of roughly 5 wt.%. This is a quite promising result. Pure manganese is prone to evaporation and the fact that a large metal particle on the surface retained this
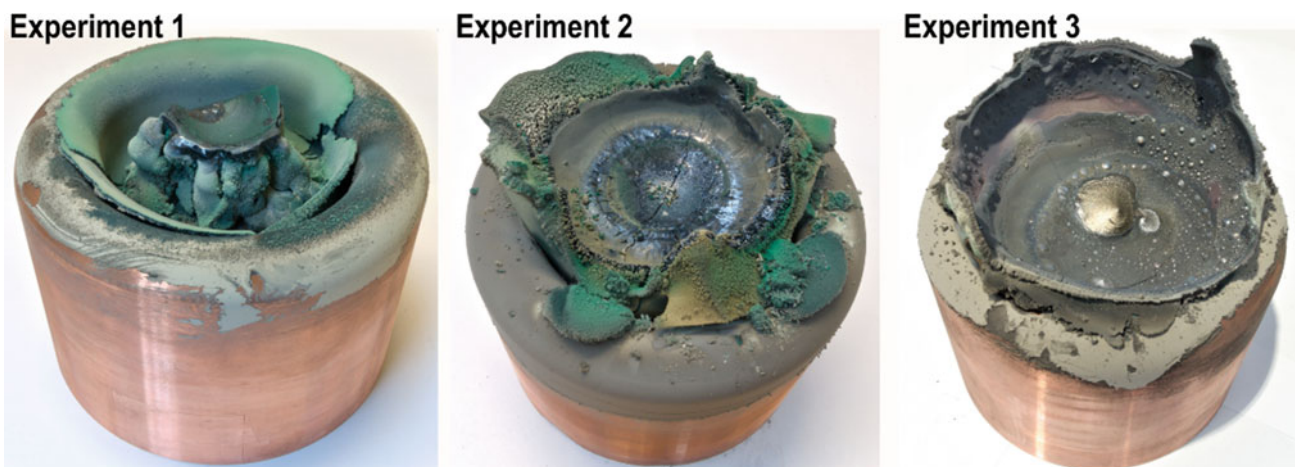
Fig. 6 Crucible and residual raw material after experiments 1–3

Fig. 7 BSE images of MnO containing metallic manganese (the dark gray phase is MnO and the lighter phase is manganese or FeMn). (**a**) Overview image of manganese formation for experiment 2; (**b**) close-up of a manganese droplet from experiment 2; (**c**) image of the main FeMn particle formed during experiment 3 containing roughly 5 wt.% manganese; (**d**) image of smaller FeMn particles with spot analysis. Spots a and e had 22 and 18 wt.% manganese, respectively, while particles deeper in the MnO matrix had only 5 wt.% manganese
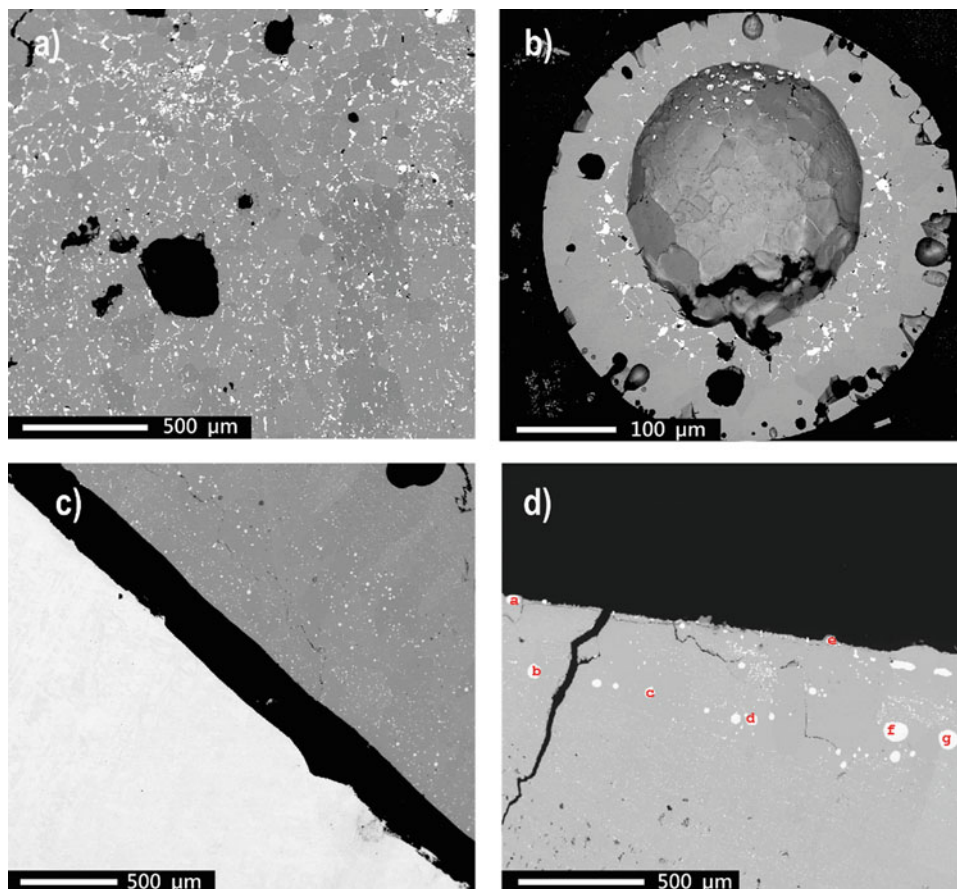
amount of manganese either means that either, the FeMn phase had lower evaporation rate than the pure manganese formed in experiments 1 and 2, or that the manganese formation rate is sufficiently high to balance the evaporation rate. Regardless of which of these statements are true, it is clear that iron has a beneficial effect.

While most of the metallic manganese formed in Experiment 3 was found in the large pool of metal or within the MnO matrix, it was seen that the manganese on the surface had a higher manganese content. Spot analysis a and e from Fig. 7d contained 22 and 18 wt.% manganese, respectively, while the other spots all had around 5 wt.% manganese. This could be because manganese forms close to the surface, at a relatively high manganese content, but is pulled into the MnO matrix due to coalescence with iron particles. If so, FeMn particles can coalesce into larger metal particles, such as the one seen in Figs. 6 and 7c.

There are two benefits achieved by producing an alloy instead of pure manganese. Firstly, the activity of manganese in an alloy is reduced. This is due to dilution, but also because the activity coefficient of manganese is lowered by the presence of iron. This leads reduced evaporation of manganese. Secondly, reducing the activity also shifts the equilibrium for the reduction reaction, which is given be Eq. (4). If the activity of manganese is lowered, Eq. (3) must be shifted to the left to maintain value of the equilibrium constant. This will increase the partial pressure of water and decrease the partial pressure of hydrogen, which is achieved by reducing MnO.

$$K = \frac{a_{Mn}p_{H_2O}}{a_{MnO}p_{H_2}} \tag{4}$$

Condensate Formation A large amount of MnO condensate was produced during the experiments. Three different types of condensates were observed during postexperimental analysis. Large condensate structures were forming on the plasma torch, and on the crucible rim. A powdery condensate was found on the reactor walls. The powdery condensate contained very fine MnO particles, in addition to a dendritic MnO structure. According to the CFD model (see Fig. 4), the gaseous products first move along the crucible rim and the plasma torch. This may explain the growth of large structures of MnO, since further away from the plasma jet the temperature drops rapidly, which allows MnO particles to form within the gas phase. Small MnO particles follow the gas flow until they are deposited on the reactor walls; however, some of them may collide and agglomerate within the gas phase and produce larger structures prior to attaching themselves to the reactor walls.

There are two main mechanisms considered for MnO condensate formation: (1) The plasma reduces MnO to manganese, but the intense heating immediately causes it to evaporate. Vaporized manganese reacts with water to produce MnO condensate; and (2) MnO evaporates directly and condenses when cooled below its boiling point. In experiment 3, it was observed through the camera feed that a significantly greater amount of smoke/dust was released from melt than in the other experiments. In addition, a greater amount of condensate formation was observed. Experiment 3 was run with higher electrical power than the two other experiments, and this suggests that the condensate is mainly due to evaporation of MnO, since a higher temperature is not expected to increase the formation of manganese notably. This can be seen by the line for reduction of MnO and H_2O being almost parallel in Fig. 1.

5   Conclusions

This work demonstrated that plasma can be used to reduce MnO with hydrogen. At this early stage, three main challenges are identified: (1) Back-reaction of manganese to MnO; (2) evaporation of MnO and excessive condensate formation; and (3) difficulties associated with the extraction of small, metallic manganese particles dispersed in the MnO matrix.

While back-reaction is anticipated as a concern, it is not yet known to what extent. Differentiating between solid MnO formed by back-reaction on one side, and precipitation of vaporized MnO on the other is not straightforward, but it will be a focus in the continuation of this work.

Adding iron to the MnO raw material was found to have a beneficial effect. This resulted in the production of a relatively large manganese-rich FeMn alloy particle (5 wt.% manganese). Despite being directly exposed to the plasma jet, the metal particle was not depleted of manganese after the experiment. This is promising and suggests that the production of ferromanganese alloys instead of pure manganese could be a good strategy.

While the results presented in this work are only a proof of concept, they nevertheless show great promise. The use of hydrogen in the production of manganese holds potential for sustainable metal production. There are, however, many unanswered questions regarding optimization of the process. Some answers are expected to be found in the continuation of the current work, when larger quantities of metal have been produced and better understanding of the back-reaction is established.

References

1. Pei M, Petäjäniemi M, Regnell A, Wijk O (2020) Toward a fossil-free future with HYBRIT: development of iron and steelmaking technology in Sweden and Finland. Metals 10(7):972. https://doi.org/10.3390/met10070972
2. Luidold S, Antrekowitsch H (2007) Hydrogen as a reducing agent: state-of-the-art science and technology. JOM 59(6):20–26. https://doi.org/10.1007/s11837-007-0072-x
3. Sabat KC, Rajput P, Paramguru RK, Bhoi B, Mishra BK (2014) Reduction of oxide minerals by hydrogen plasma: an overview. Plasma Chem Plasma Process 34(1):1–23. https://doi.org/10.1007/s11090-013-9484-2
4. Filho IR et al (2021) Sustainable steel through hydrogen plasma reduction of iron ore: process, kinetics, microstructure, chemistry. Acta Mater 213:116971. https://doi.org/10.1016/j.actamat.2021.116971
5. Jensen R, van der Eijk C, Wærnes AN (2021) Production of sustainable hydrogen and carbon for the metallurgical industry. Mater Proc 5(1):1. https://doi.org/10.3390/materproc2021005067
6. Antrekowitsch J, Wibner S, Hanke G (2023) Hydrogen, a promising carbon substitute in metallurgy? In: Advances in pyrometallurgy, Cham, pp 27–34. https://doi.org/10.1007/978-3-031-22634-2_3
7. Dalaker H, Eldrup N, Jensen R, Kvande R (2022) Techno-economic pre-feasibility study of a hydrogen plasma-based ferromanganese plant. In: REWAS 2022: developing tomorrow's technical cycles, vol I, Cham, pp 647–658. https://doi.org/10.1007/978-3-030-92563-5_68
8. Dalaker H, Hovig EW (2023) Hydrogen plasma-based reduction of metal oxides. In: Advances in pyrometallurgy, Cham, pp 85–94. https://doi.org/10.1007/978-3-031-22634-2_8
9. Dalaker H, Aarnæs TS, Jensen R, Johnsen S (2023) Manganese production from MnO by use of hydrogen plasma. In: Presented at the 25th international symposium on plasma chemistry, Kyoto, Japan
10. 'ANSYS Fluent 2022R1'. [Online]. Available: http://www.ansys.com
11. Boulos M, Fauchais P, Pfender E (1994) Thermal plasmas: fundamentals and applications, 1st edn. Springer, New York
12. Liani B, Rahmouni M, Belbachir AH, Riad H, Gleizes A (1997) Computation of net emission of – thermal plasmas. J Phys Appl Phys 30(21):2964. https://doi.org/10.1088/0022-3727/30/21/010
13. Aubrecht V, Bartlova M, Bogatyreva N (2009) Radiation properties of argon thermal plasma in various spectral regions. In: Presented at the 29th international conference on phenomena in ionized gases, Cancun, Mexico
14. Johnsen S, Simonsen A (2014) CFD modeling of a rotating arc plasma reactor. In: 10th international conference on CFD in oil & gas, metallurgical and process industries, Trondheim, Norway. https://doi.org/10.13140/RG.2.2.20874.13768